

Electrocatalytic membrane with *p*-block bismuth atoms for selective oxygen activation to hydroxyl radicals for effective water decontamination

Limin Jin ^{a,b}, Meng Liu ^a, Shijie You ^c, Hongying Zhao ^d, Yanbiao Liu ^{a,b,*}

^a School of Environmental Science and Technology, Key Laboratory of Industrial Ecology and Environmental Engineering (Ministry of Education), Dalian University of Technology, Dalian POCT Laboratory, Dalian, China

^b College of Environmental Science and Engineering, Donghua University, Shanghai 201620, China

^c State Key Laboratory of Urban Water Resource and Environment, School of Environment, Harbin Institute of Technology, Harbin, Heilongjiang 150090, China

^d Shanghai Key Lab of Chemical Assessment and Sustainability, Key Laboratory of Yangtze River Water Environment, School of Chemical Science and Engineering, Tongji University, 1239 Siping Road, Shanghai 200092, China



ARTICLE INFO

Keywords:

p-Block bismuth
Electrocatalytic membrane
Oxygen reduction reaction
Hydroxyl radicals
Water purification

ABSTRACT

Herein, individual *p*-block bismuth (Bi) atoms are dispersed onto N-doped $Ti_3C_2T_x$ MXene ($BiN_3/MXene$) to enhance the $3e^-$ oxygen reduction reaction (ORR), for the electrosynthesis of hydroxyl radicals (HO^\bullet) via the activation of molecular oxygen (O_2). Theoretical calculations and experiments reveal that the *p*-orbitals of Bi atoms can readily hybridize with the *p*-orbitals of O, which enables the transfer of charges, creates sufficient strength of adsorption for oxygen intermediates, lowers the activation energy, and modulates the rate-limiting reaction. The optimized generation of HO^\bullet is up to $26.7 \mu\text{mol}/(\text{L}\cdot\text{h}\cdot\text{cm}^2)$ without additional chemical reagents, facilitating efficient removal of micropollutants from complex water matrices. Specifically, the rate constant (k_{obs}) for sulfamethoxazole degradation achieves 1.027 min^{-1} , outperforming the reported processes for micropollutants removal. This work illuminates the atomic-level construction of a *p*-block $BiN_3/MXene$ electrocatalytic membrane to efficiently perform the $3e^-$ ORR and highlights the substantial potential for wastewater decontamination.

1. Introduction

There is an urgent need to develop effective and sustainable strategies to mitigate water pollution [1–3]. Electro-Fenton technology, which uses molecular oxygen (O_2) as a reactant, has garnered significant attention because of the non-polluting properties of hydrogen peroxide (H_2O_2) and the capability for *in situ* generation of reactive oxygen species (ROS) [4,5]. Notably, hydroxyl radicals (HO^\bullet) have emerged as a favorable candidate for destroying, deactivating, or transforming trace level micropollutants (ng/L to $\mu\text{g}/\text{L}$) into inert and less concerning products because of their robust oxidizing properties ($E_0 = 2.80 \text{ V}_{\text{NHE}}$) [6]. However, there are fundamental challenges with the electro-Fenton process, including the absence of selective and active catalysts for the formation of H_2O_2 via a $2e^-$ oxygen reduction reaction (ORR), the low efficiency of H_2O_2 decomposition through the Haber-Weiss cycle, and the sluggish kinetics for the cycling of active metal sites [7–9]. Thus, the general appreciation of the advantages of the electro-Fenton process has

motivated researchers to develop effective and sustainable strategies for producing HO^\bullet .

Recently, electrocatalytic membranes, which seamlessly integrate catalytic processes and electrochemistry, have drawn considerable consideration, offering compelling advantages for wastewater decontamination [10,11]. During the membrane process, ROS can be generated through catalytic reactions that involve only oxygen and water and free of chemical inputs [12,13]. Additionally, these processes could be operated with electricity generated from renewable sources. However, the removal efficiency of micropollutants using membranes affixed with metal oxide catalysts has typically been unsatisfactory, primarily because of the weak reactivity of the electrocatalysts and their poor yield of ROS. One potentially potent strategy for the electrocatalytic generation of ROS relies on the construction of single atom catalysts (SACs) on the membranes surface, which maximizes the utilization of the SACs and their adjustable electronic structures [14,15]. Additionally, laminar membranes that are spatially constrained by channels can

* Corresponding author at: School of Environmental Science and Technology, Key Laboratory of Industrial Ecology and Environmental Engineering (Ministry of Education), Dalian University of Technology, Dalian POCT Laboratory, Dalian, China.

E-mail address: yanbiaoliu@dhu.edu.cn (Y. Liu).

improve mass transfer by minimizing the distance for diffusion, aligning the flow of the ROS and the micropollutants, thereby enhancing the overall reaction kinetics.

Fortunately, strategically engineered SACs on membranes can boost the $2e^-$ ORR and subsequently effectively activate H_2O_2 to form HO^\bullet via the $1e^-$ ORR, improving the degradation efficiency and system stability [16,17]. The scientific bottlenecks in the $3e^-$ ORR predominantly arise from orbital interactions between reaction intermediates and active sites during the electrochemistry processes. Substantial advancements have been achieved in the electrocatalytic performance by tailoring the coordination environment in the form of N-coordinated metals (M-N_x) [18, 19]. However, the M-N_x SACs primarily used *d*-block metal atoms (e.g., Fe, Co, and Ni) that typically have *d*-electron bands and partially filled with electron energies at the Fermi level (E_F) [20]. The *p*-block metals that possess a closed d^{10} -electronic configuration and a delocalized *p*-band have difficulties binding with intermediates as host orbitals during the electron transfer process, resulting in low catalytic activities and limited studies on their use [21]. Excitingly, recent findings have demonstrated that the *s*- and *p*-electrons of *s*- and *p*-block metals filled with d^{10} -orbitals can become catalytically active by forming single-metal M-N_x matrices, with impressive electrocatalytic performance [22,23]. Among *p*-block elements, bismuth (Bi) has been noted for its strong affinity to O₂ and oxylated moieties through electrostatic attraction [24]. It was, thus, reasonable to hypothesize that the ORR activity of Bi active sites can be fine-tune by regulating the occupied state of *p*-orbital electrons within Bi atoms. Furthermore, Bi metals are priced comparably to copper (Cu) [25], positioning them as promising alternatives for the deliberate design of advanced electrocatalytic systems targeting environmental applications.

In this research, we systematically designed and constructed *p*-block Bi-SACs on N-doped Ti₃C₂T_x MXene to enhance the reducibility and selectivity of O₂ conversion into HO[•] during the electrochemical route. The Bi-SACs, in conjunction with the ordered MXene structure, guaranteed the formation of an excess functionally reactive sites as well as enhanced reactant transport in the electrocatalytic filtration system toward effective sulfamethoxazole (SMX) degradation. As demonstrated with a combination of experimental results and theoretical calculations, the distinctive Bi-N₃ configuration facilitated the selective generation of *H₂O₂ intermediates and regulated both the adsorption energy and activation energy of *H₂O₂, which ultimately expedited the generation of HO[•] in the $3e^-$ system of O₂ activation. The optimal generation of HO[•] reached 26.7 $\mu\text{mol}/(\text{L}\cdot\text{h}\cdot\text{cm}^2)$ using only the BiN₃/MXene membrane without additional chemical reagents. This work highlights a distinctive electrochemistry strategy to enhance chemoselectivity by synthesizing HO[•] that could be applied in a wide array of conditions for the treatment of polluted environments.

2. Experimental section

2.1. Synthesis of the BiN₃/MXene electrocatalytic membrane

All reagents and chemicals were analytical grade and used without further purification (Text S1). Ti₃C₂T_x MXene nanosheets were prepared by etching the Al layer from Ti₃AlC₂ in an HCl/LiF solution (Text S2), as described previously [26]. First, 2.0 g of melamine was vigorously stirred in 30.0 mL of absolute ethanol for 1 h. Subsequently, 3.0 mL of HCl (37 wt%), serving as protonation reagent, was added to the mixture and stirred for another 1 h. The stirred mixture was washed and centrifuged repeatedly with deionized water and ethanol before being transferred into an oven for solvent vaporization. Typically, 200.0 mg of melamine was added into 50.0 mL of MXene colloidal suspension (1.0 mg/mL). The positively charged melamine tended to be absorbed onto the surface of MXene nanosheets and induced colloidal coagulation. Next, 5.0 mL of Bi(NO₃)₂·5 H₂O (2.0 mg/mL) was slowly added to the mixture while vigorously stirring and ultrasonication for 30 min in ice bath. After freeze-drying for 12 h, the obtained mixture was annealed

at 350 °C in N₂ atmosphere for 4 h. A 30.0 mg of the produced BiN₃/MXene powder was mixed in 40.0 mL of deionized water and sonicated for 30 min to create a homogeneous suspension that could be used to fabricate a free-standing BiN₃/MXene membrane *via* vacuum filtration onto a poly(tetrafluoroethylene) substrate. Details on the characterization are available in Text S3.

2.2. Experimental setup

All electrocatalytic degradation experiments were conducted with a commercially available Whatman polycarbonate filtration system that was modified for electrochemistry applications [27,28]. A perforated Ti sheet and the BiN₃/MXene membrane served as anode and cathode, respectively, with a typical working area of 7.1 cm². The electric field was supplied by a DC power source (DH1766A-1, China) under constant current mode at 10.0 mA. To eliminate any contribution from adsorption on the micropollutants degradation, adsorption saturation of all membranes was achieved prior to exerting an electric current. The reaction solution containing 20.0 mmol/L Na₂SO₄ and 10.0 mg/L SMX was recirculated through the filter at flow rate of 6.0 mL/min, and O₂ was introduced at 100.0 mL/min to initiate electrolysis. Exhausted BiN₃/MXene membrane was collected, washed with deionized water, dried in a vacuum oven for 4 h at 50 °C, and then used for cycling tests to evaluate the stability.

2.3. Analytical equipment

The concentration of H₂O₂ generated during the electrolysis process was quantified by a colorimetric protocol [29]. The content of HO[•] could be determined by the photoluminescence signal of hydroxybenzoic acid, obtained from the capture of HO[•] by benzoic acid [30]. The concentration of SMX was analyzed with an HPLC (Shimadzu LC-20A) at a wavelength of 286 nm. SMX degradation intermediates were identified by ultrahigh performance liquid chromatography-quadrupole time-of-flight mass spectrometry (UPLC-QTOF-MS) on a LC/Q-TOF system (Agilent). The ROS species were analyzed with an electron paramagnetic resonance (EPR) spectrometer (Bruker EMXnano) with 5,5-dimethyl-1-pyrroline (DMPO) or 2,2,6,6-tetramethyl-4-piperidinol (TEMP) functioning as the spin-trapping agents. Electrochemical tests were conducted on a CHI 760E electrochemical system (China) with a three-electrode measurement cell. Detailed procedures are available in Text S4 ~ S7.

3. Results and discussion

3.1. Characterization of BiN₃/MXene electrocatalytic membrane

As schematically depicted in Fig. 1a, the BiN₃/MXene electrocatalytic membrane was prepared using melamine and Bi(NO₃)₂·5 H₂O as the N and Bi sources, respectively. Of the generated samples, a BiN₃/MXene system with a theoretical Bi loading of 4.0% exhibited the highest electrocatalytic activity, thus being selected as model material for subsequent study (Fig. S1). Analysis of the BiN₃/MXene with XRD patterns revealed a crystal structure resembling that of pristine MXene, without detecting a Bi crystalline phase, implying the absence of Bi-based clusters or nanoparticles (Fig. 1b) [31]. Notably, the main peaks of the BiN₃/MXene sample were slightly shifted toward a lower angle compared to that of pristine MXene (inset). Analysis with high-resolution TEM determined that the width of BiN₃/MXene was about 200 ~ 500 nm and no Bi nanoparticles were observed (Fig. 1c), consistent with the XRD results. The use of HAADF-STEM confirmed that the lattice fringes matched well with the crystal planes of the MXene nanosheets (Fig. 1d) [32]. Notably, the brightness of the atomic columns from the HAADF-STEM image correlated with the atomic number (Bi > Ti), such that the high-intensity spots of the green cycle correspond to the single Bi atoms on the MXene matrix. Analysis of the line intensity

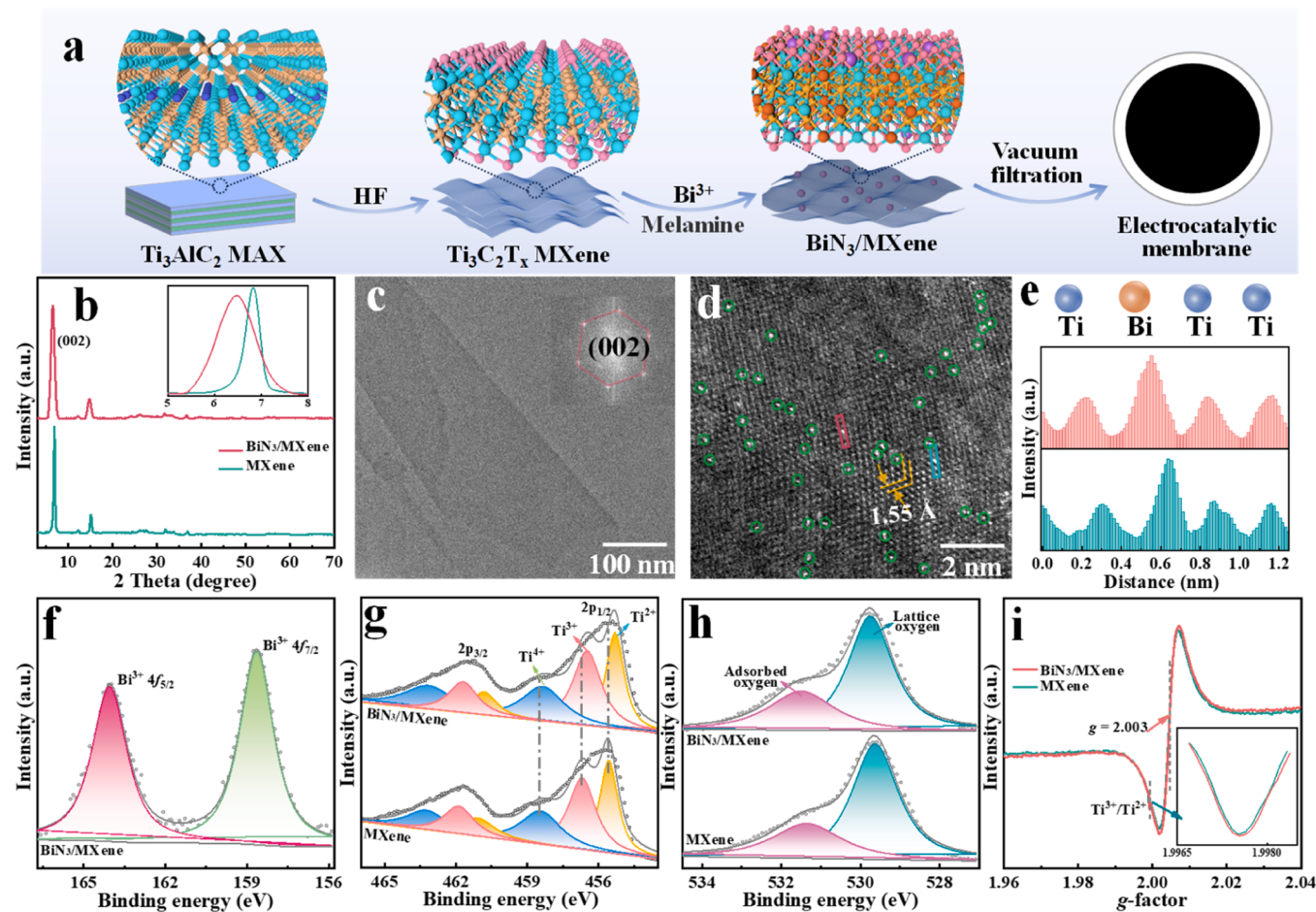


Fig. 1. Synthesis and characterization of the BiN₃/MXene membrane. (a) Schematic illustration of the preparation of BiN₃/MXene membrane. (b) XRD patterns of MXene and BiN₃/MXene. (c) High-resolution TEM image of BiN₃/MXene. (d) Atomic-scale-resolution HAADF-STEM image of BiN₃/MXene. (e) The line scan from the HAADF-STEM image taken along the x-y rectangular regions. XPS spectra for (f) Bi 4f, (g) Ti 2p, and (h) O 1s of BiN₃/MXene. (i) EPR signals of MXene and BiN₃/MXene.

profiles verified that individual Ti atoms were replaced by Bi atoms in the structure (Fig. 1e), indicating the formation of Bi–N(O)–Ti configuration. Furthermore, the cross-section FESEM image of the BiN₃/MXene membrane demonstrated a typical laminar structure with uniform 2D nanochannels and typical thickness of 95.0 ± 5 μm (Fig. S2).

As displayed in Fig. 1f, the XPS binding energy of Bi 4f for BiN₃/MXene (Bi³⁺ 4f_{7/2} at 158.5 eV and Bi³⁺ 4f_{5/2} at 163.8 eV) possessed an obvious negative shift of ~ 0.2 eV compared with commercial Bi₂O₃ (Bi³⁺ 4f_{7/2} at 158.7 eV and Bi³⁺ 4f_{5/2} at 164.0 eV), indicating the electronic redistribution between decorated Bi and N species on MXene matrix [33]. Notably, the Ti 2p_{3/2} peak of BiN₃/MXene exhibited a positive shift of ~ 0.4 eV compared to MXene, further indicating that the Ti atoms acted as electron donors and transferred electrons from Ti to Bi species in the Bi–N(O)–Ti structure (Fig. 1g). The O 1s peaks of the XPS spectrum of BiN₃/MXene (Fig. 1h) that were centered at 530.3 and 531.5 eV were assigned to the lattice and adsorbed O species. Additionally, the BiN₃/MXene had a strong EPR signal at *g* = 2.003 because of the free electrons provided by O vacancies (Fig. 1i), while weak EPR signals at *g* = 1.997 could be due to unpaired electrons arising from the lower oxidation states of Ti (Ti³⁺ and Ti²⁺) [34,35], as indicated by the XPS analysis.

XANES and EXAFS were used to analyze the local electronic coordination of the Bi atoms anchored on the MXene support [36]. The XANES curves of the Bi *L*₃-edge (Fig. 2a) show that the absorption threshold of BiN₃/MXene appeared at a lower energy compared to Bi₂O₃, indicating that the charge transfer in BiN₃/MXene led to a

decrease in the average valence state of the Bi³⁺ ($\delta > 0$) species [37]. A Fourier transform (FT), weighted by k^2 , of the EXAFS (Fig. 2b) exhibited a dominant peak that was assigned to Bi–N coordination at ~ 1.60 Å, which was almost identical to the Bi–O peak of Bi₂O₃ (~ 1.65 Å) [38]. Additionally, no Bi–Bi/Bi–O(C)–Bi coordination was detected in BiN₃/MXene, once again indicating the presence of distinct Bi atoms attached to the MXene via the Bi–N bonding. The use of a wavelet-transform EXAFS (WT-EXAFS) on the results enabled back-scattering atoms to be distinguished (Fig. 2c). Unlike the WT-EXAFS plots of Bi₂O₃ (Bi–Bi and Bi–O scattering paths at ~ 8.5 and ~ 4.6 Å⁻¹, respectively) and Bi foil (Bi–Bi scattering path at ~ 9.0 Å⁻¹), a single dominant peak attributable to the Bi–N scattering at ~ 4.0 Å⁻¹ was apparent for the BiN₃/MXene sample [39], further confirming the presence of isolated Bi atoms fixed on the MXene support. Additionally, the bond length between the Bi and N atoms in the BiN₃/MXene increased compared to pristine Bi₂O₃, consequently leading to an expansion in the Bi–N–Bi bond length, as depicted in Fig. 2d. Based on the fitting results derived from the FT-EXAFS curves (Fig. 2e), the main peak at 1.6 Å can be assigned to the nearest coordination shell of the N of BiN₃/MXene, while the minor bulge at ~ 2.2 Å was associated with scattering path of the second shell of Ti. The coordination numbers for the Bi atoms in BiN₃/MXene were determined to be 2.7 ± 0.2 at distances of 2.18 ± 0.01 Å (Table S1), thus, forming a typical Bi–N₃ configuration. All results comprehensively validated the distinctive local atomic configuration in the BiN₃/MXene membrane.

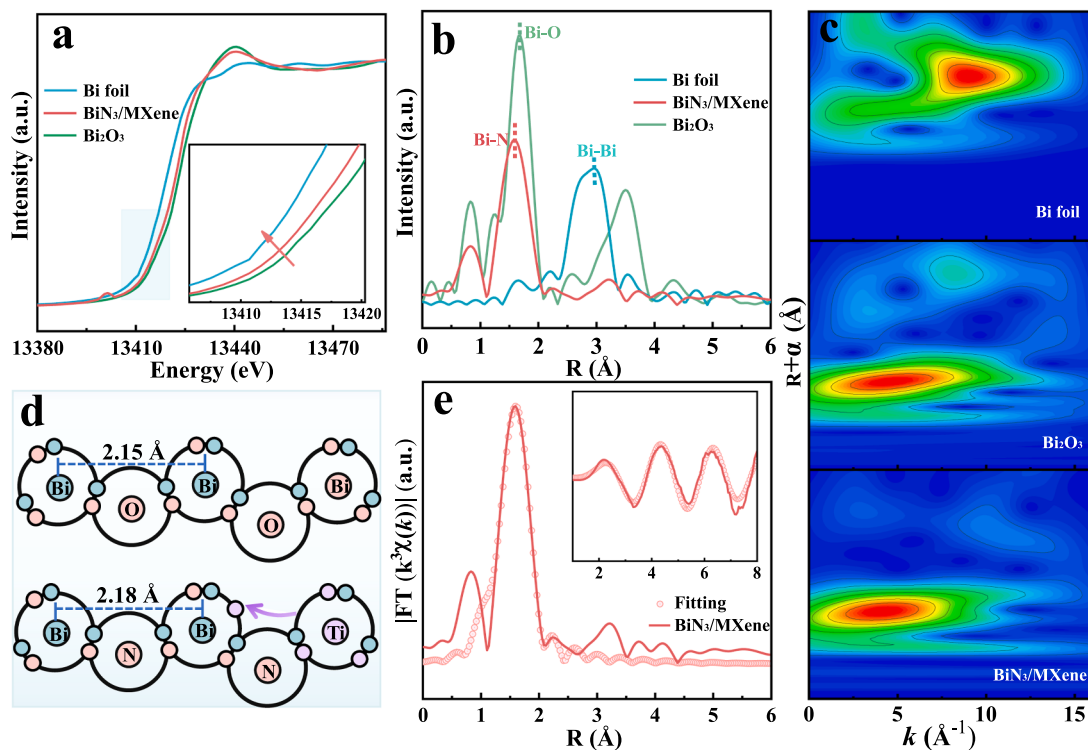


Fig. 2. Structure characterization of BiN₃/MXene membrane and reference materials for comparison. (a) Normalized Bi L₃-edge XANES. (b) FT-EXAFS spectra. (c) WT-EXAFS spectra. (d) Schematic of the local structure change after Bi modification. (e) EXAFS fitting curves of BiN₃/MXene in R space (Inset: k space-fitting curves).

3.2. Evaluation of electrocatalytic performance

The electrocatalytic capacity of the BiN₃/MXene electrocatalytic membrane for the activation of O₂ was evaluated using a series of electrochemical characterizations. As shown in Fig. S3, the circular arc related to the BiN₃/MXene exhibited a lower radius than that of pristine MXene by means of electrochemical impedance spectroscopy (EIS), implying that the addition of Bi-N₃ sites remarkably decreased the interfacial resistance and accelerated the interfacial electron transfer process. Cyclic voltammetry (CV) curves of BiN₃/MXene revealed a more distinct reduction peak in the O₂-saturated solution compared to the pristine MXene (Fig. 3a). In contrast, the peak was absent in the N₂-saturated solution, indicating the remarkable role of Bi-N₃ sites for the enhanced activation of O₂. Linear sweep voltammetry (LSV, Fig. 3b) showed that the BiN₃/MXene had a higher onset potential (E_{onset} = 0.82 V vs. RHE) than the pristine MXene (E_{onset} = 0.76 V vs. RHE). As illustrated in Fig. 3c, the BiN₃/MXene exhibited a lower Tafel slope (36.2 mV/dec) extracted from the LSV curve, providing evidence of the enhanced kinetics for the activation of O₂ compared to MXene. According to the ring current density (Fig. 3d, e) from the rotating ring-disk electrode (RRDE) measurements, the average number of transferred electrons for O₂ activation by the BiN₃/MXene system was determined to be ~ 2.9 at 0.0 ~ 0.2 V vs. RHE, leading to a much lower selectivity for H₂O₂ (~ 55%), which may be caused by the one-electron reduction route of H₂O₂ [6,40]. Additionally, the H₂O₂ concentration in the BiN₃/MXene system (~ 2.7 mmol/L) was similar to that of MXene-alone system (~ 2.1 mmol/L) based on the RRDE measurements (Fig. S4). This was attributed to activation and desorption of H₂O₂, inferring the occurrence of the 3e⁻ ORR in the BiN₃/MXene system.

To verify the generation and activation of oxygenated intermediates, EPR spectroscopy was employed to investigate the effect of Bi-N₃ sites and O vacancies on the MXene matrix for O₂ activation. As shown in Fig. 3f, the intensity of the DMPO-HO[•] signal in the MXene system was much lower than that in the BiN₃/MXene system under N₂-saturated and natural conditions (Fig. S5) with addition of 1.0 mmol/L H₂O₂,

respectively, suggesting that the electro-Fenton reaction occurred among the Bi-N₃ sites, O vacancies, and oxygenated intermediates [41]. An LSV curve was generated with and without the addition of H₂O₂ under the N₂-saturated condition. As presented in Fig. 3g, both the BiN₃/MXene and MXene displayed a near E_{onset} of 0.8 V vs. RHE, while the current density in the BiN₃/MXene system was higher than that of the MXene system, emphasizing the remarkable impact of the Bi-N₃ sites on the activation process of the oxygenated intermediates. Benzoic acid and coumarin were selected as the probe molecules to detect the formation of HO[•] based on their different solubilities in aqueous solutions [42]. In Fig. 3h, the overall concentration of HO[•] in the BiN₃/MXene system was markedly increased in the presence of the benzoic acid probe, which had good solubility and a carboxyl group. Conversely, the concentration of HO[•] in the solution decreased with the coumarin probe, which had lower solubility (Fig. 3i), indicating that the accumulated HO[•] was predominantly situated on the membrane surface. These results collectively demonstrated that the BiN₃/MXene electrocatalytic system could enhance the reducibility and selectivity of O₂, thus facilitating an efficient HO[•] yield.

SMX was chosen as an exemplar pollutant to test the electrocatalytic capability of the as-synthesized membranes for the conversion of O₂ to HO[•]. As shown in Fig. 4a, only 15.0% of SMX was eliminated when it was treated with the pristine MXene for 40 min, while 100% of SMX was eliminated when the BiN₃/MXene was used under similar conditions, demonstrating the positive effect of the Bi-N₃ sites for micropollutants decontamination. To facilitate a comprehensive comparison of electrocatalytic performance, a pseudo-first order observed rate constant (k_{obs}) of 1.027 min⁻¹ ($R^2 = 0.991$) was determined for SMX degradation by the BiN₃/MXene system, almost 35 × greater than that of the MXene system (Fig. S6). The contribution of physical adsorption and electrochemical adsorption for SMX removal were insignificant, 5% and 8% using BiN₃/MXene system within 40 min, respectively (Fig. S7). This indicated that SMX degradation was primarily caused by the BiN₃/MXene electrocatalytic system in an O₂-saturated condition. To determine the major ROS responsible for SMX degradation in the BiN₃/

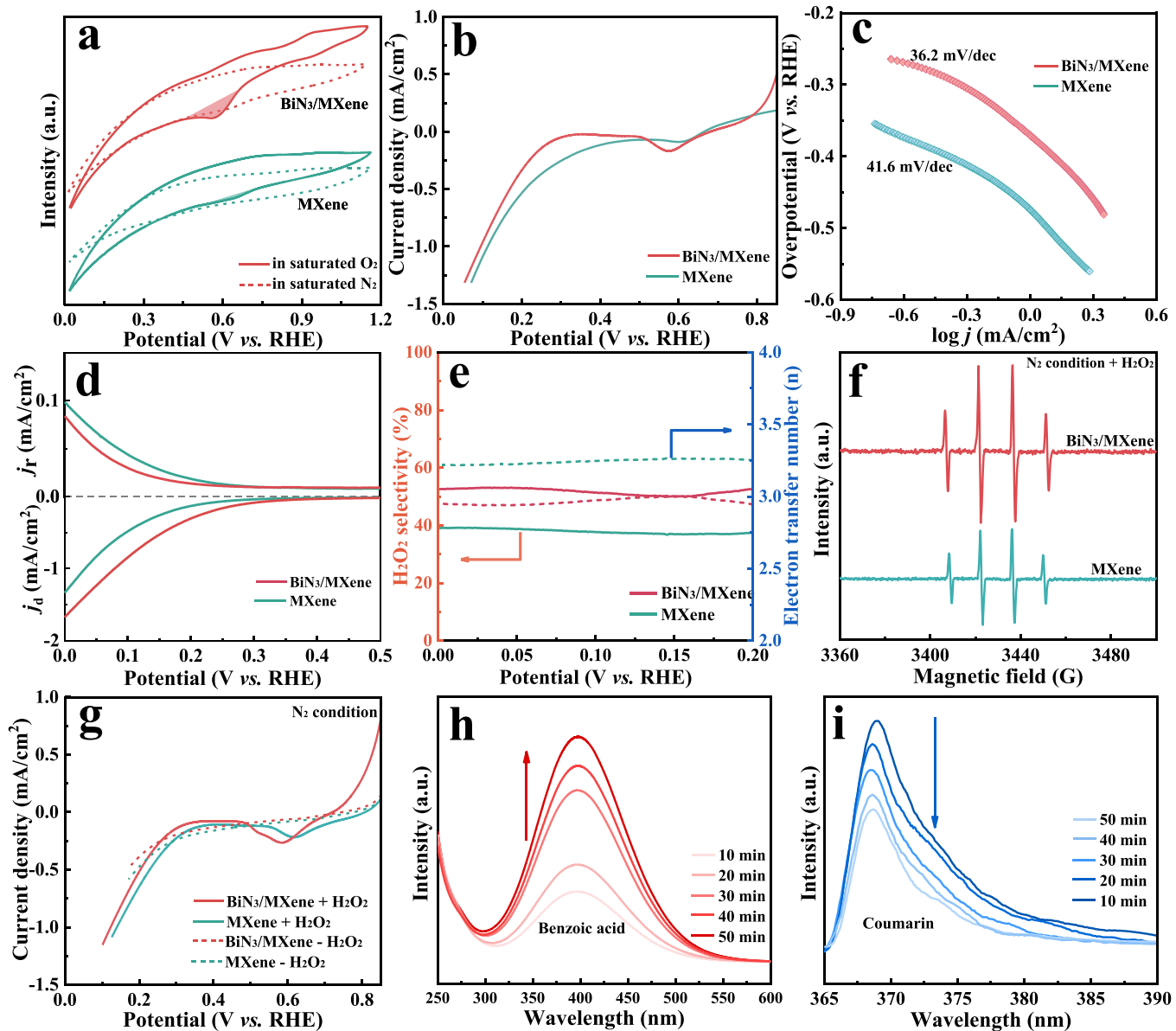


Fig. 3. Electrocatalytic performance evaluations of $\text{BiN}_3/\text{MXene}$ membranes. (a) CV curves. (b) LSV curves. (c) Tafel slope. (d) RRDE polarization curves. (e) The calculated H_2O_2 selectivity and electron transfer number. (f) EPR spectra. (g) LSV curves of MXene and $\text{BiN}_3/\text{MXene}$ membranes. (h) Benzoic acid and (i) coumarin fluorescence spectra for HO^\bullet detection in $\text{BiN}_3/\text{MXene}$ system.

MXene system, quenching experiments were conducted using different trapping agents. As shown in Fig. 4b, the introduction of TBA, an HO^\bullet scavenger, caused a significant decrease of k_{obs} from 1.027 min^{-1} to 0.021 min^{-1} , proving that HO^\bullet was responsible for SMX degradation. In contrast, independent injections of superoxide dismutase (SOD), furfuryl alcohol (FFA), and catalase, which are $^*\text{OOH}$, $^1\text{O}_2$, and H_2O_2 scavengers, respectively, only slightly decreased the SMX degradation kinetics, indicating that O_2 was potentially reduced to $^*\text{OOH}$ or $^*\text{H}_2\text{O}_2$ intermediate via electron transfer, followed by the subsequent reduction to HO^\bullet . The plausible SMX degradation pathways in $\text{BiN}_3/\text{MXene}$ system were available in Fig. S8 with HO^\bullet as the dominant ROS.

To assess the electrocatalytic performance, the observed k_{obs} in the homogeneous system ($\text{Bi}^{2+}/\text{MXene}$) was determined to be 0.01 min^{-1} (Fig. 4c), where MXene served as the cathode and Bi^{2+} acted as the electrocatalyst, equivalent to the Bi content in the $\text{BiN}_3/\text{MXene}$ membrane (Text S8). Even with a 30-fold increase in Bi^{2+} concentration, the k_{obs} for SMX degradation remained less efficient than that achieved by

the $\text{BiN}_3/\text{MXene}$ system (Fig. S9), highlighting the unique advantage of the SACs. As observed in Fig. S10, the flow-through configuration exhibited a > 6 -fold increase in the SMX degradation kinetics ($k_{\text{obs}} = 1.027 \text{ min}^{-1}$) than that of batch mode ($k_{\text{obs}} = 0.017 \text{ min}^{-1}$) under similar conditions. This can be ascribed to effective convection-enhanced mass transport of confined nanofluids within the flow-through configuration, while mass transfer in the batch mode was diffusion-limited. Furthermore, the low-current electrocatalytic system treating real wastewater had a specific energy consumption of 0.05 kWh/g SMX with a constant current of 10.0 mA (Text S9), outperforming several state-of-the-art electrochemical processes (Table S2). Interestingly, the design strategy exhibited universality and feasibility in enhancing HO^\bullet generation and SMX degradation with other p -block (Sb, Sn, and Pb) elements (Fig. 4d), indicating the considerable potential for practical applications. Notably, the $\text{BiN}_3/\text{MXene}$ system had the highest intrinsic activity for SMX degradation, even outperforming many previously reported electro-driven micropollutant degradation systems by

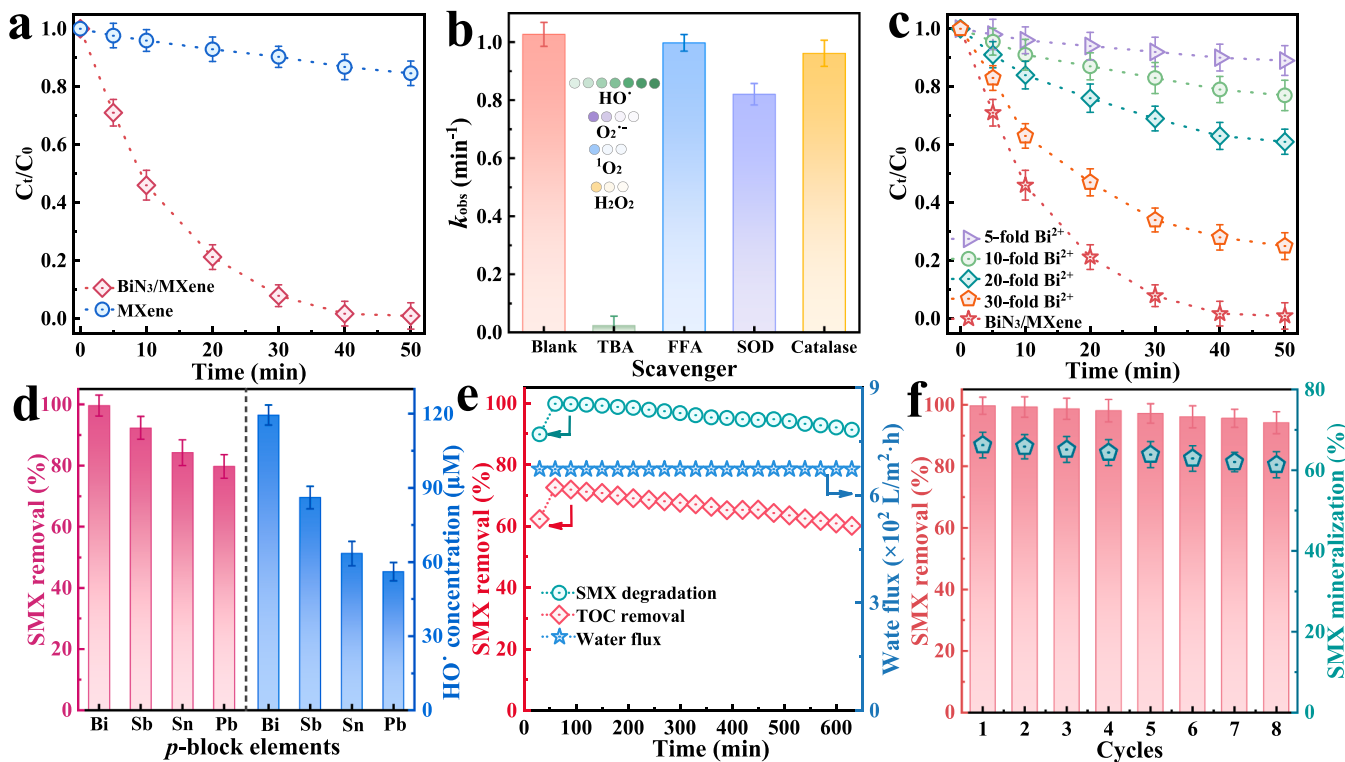


Fig. 4. Electrocatalytic degradation performance. (a) SMX degradation. (b) k_{obs} comparison in quenching experiments. (c) SMX degradation with different equivalents of Bi²⁺ as catalysts. (d) Electrocatalytic performances of p-block elements in HO[•] generation and SMX removal. (e) Long-term operation. (f) Cycle stability within the BiN₃/MXene system. Experimental conditions: flow rate = 6.0 mL/min, [SMX]₀ = 10.0 mg/L, pH = 6.8, and constant current = 10.0 mA.

d-block metals (Table S2).

To evaluate the potential utility, a continuous-flow reactor equipped with BiN₃/MXene membrane was employed to address the long-term degradation of SMX in pharmaceutical wastewater (Shanghai; Table S3). Despite a marginal decrease in membrane permeance (Fig. 4e), 90% of SMX removal and 60% of total organic carbon (TOC) removal were consistently achieved by the BiN₃/MXene system with continuous operation over 600 min, reflecting the remarkable electrocatalytic activity and durability. Additionally, the XRD and TEM results (Fig. S11) further excluded any phase transformation or reconstruction of the BiN₃/MXene after reaction, suggesting a robust metal-support interaction during the electrocatalytic process. Moreover, BiN₃/MXene system exhibited remarkable reusability, as evidenced by maintaining > 63% TOC removal in the eighth consecutive run (Fig. 4f). Remarkably, the BiN₃/MXene system could effectively remove ~ 100% of SMX from tap water, lake water, and pharmaceutical wastewater (spiked with 10.0 mg/L SMX; Fig. S12a). Similarly, the system can also be adaptable for the decontamination of other refractory organic pollutants (e.g., 2-chlorophenol, *p*-nitrophenol, bisphenol A, and sulfadiazine; > 90%; Fig. S12b). Furthermore, the removal efficiency > 95% of SMX were obtained across a wide pH range of 3.0 ~ 9.5 (Fig. S13a) in the BiN₃/MXene system, surpassing the pH limitation of traditional *d*-block O₂-activation systems [43]. However, the solution pH of effluent increased due to the rapid elimination of O₂ accompanied by the accumulation of OH⁻ anions (O₂ + 2 H⁺ + 3e⁻ → OH⁻ + HO[•]; Fig. S13b) [44]. The results demonstrated that the homogeneous (high catalytic activity) and heterogeneous (facile post-reaction recovery) design of the electrocatalytic membrane had good potential for micropollutants remediation from water.

3.3. Electrocatalytic mechanism

A quantitative analysis was initially performed to determine the conversion efficiency of O₂ and the ratio of distinct oxygenated species

in BiN₃/MXene system. As shown in Fig. 5a, the concentration of dissolved O₂ decreased from 213.6 to 19.2 μmol/L within 40 min, while the concentrations of HO[•], H₂O₂, ¹O₂, and O₂^{•-} in the aqueous solution were 119.7, 2.2, 0.3, and 0.1 μmol/L, respectively, highlighting that HO[•] was the primary ROS in the O₂ activation process. Thus, the ratios of HO[•], H₂O₂, ¹O₂, and O₂^{•-} with the total ROS were 97.88, 1.79, 0.25, and 0.08%, respectively (Fig. 5b). However, the DMPO-O₂^{•-} signal was hardly detected with EPR spectroscopy (Fig. S14), indicating the near-complete utilization of O₂^{•-} in the ORR. Additionally, the ¹⁸O₂ isotope-labeling technique was employed to identify the oxygenated intermediates, providing insights into the O₂ activation pathway from ATR-FTIR spectroscopy. As depicted in Fig. 5c, two distinct peaks at 1030.1 and 1222.5 cm⁻¹ appeared in the BiN₃/MXene system with the ¹⁸O₂-saturated electrolyte, corresponding to *H₂O₂ and *OOH intermediates, respectively [45]. Conversely, the same characteristic peaks exhibited a noticeable shift towards higher wavenumbers in ¹⁶O₂-saturated conditions due to changes in the O–O stretching vibration of the *H₂O₂ and *OOH species. Combined with the EPR results under N₂-saturated condition (Fig. S15), it was concluded that the O atoms constituting *in situ* formed O₂^{•-} and H₂O₂ intermediates were derived from O₂.

To explore the fundamental parts of the O₂ conversion into HO[•] with electrocatalysis, Raman spectra were collected to thoroughly investigate the adsorbed intermediates and the reaction pathways. As shown in Fig. 5d, three noticeable peaks were detected at 563, 632, and 1091 cm⁻¹, which corresponded to the stretching vibration of Bi–O in the Bi–OH, Bi–OOH, and Bi–O₂ species, respectively, in the BiN₃/MXene system. Conversely, distinct peaks were only observed with the addition of H₂O₂ in the MXene system, suggesting that the Bi–N₃ sites and O vacancies on the MXene were responsible for the O₂ activation. Additionally, the increased Bi–O stretching vibration of the Bi–OOH species coupled with the diminished Bi–O stretching vibration of the Bi–OH species in BiN₃/MXene system (Fig. 5e), indicated that *OOH intermediates rather than *H₂O played a dominant role in HO[•] generation.

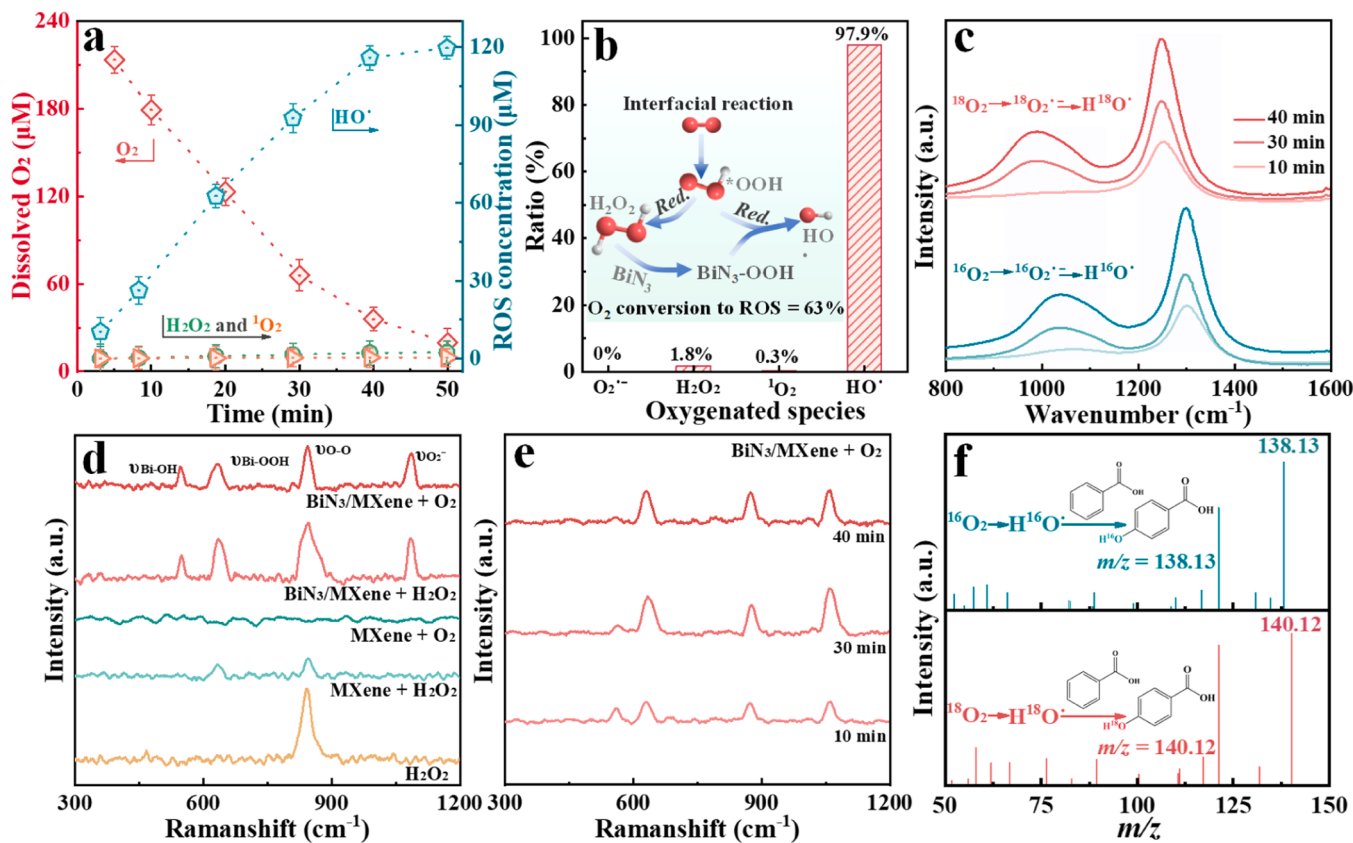


Fig. 5. Mechanism investigation of 3e[−] ORR in BiN₃/MXene system. (a) Quantitative determination of the dissolved O₂ and generated ROS. (b) The ratio of O₂ to individual ROS. (c) ATR-FTIR spectra in ¹⁸O₂- and ¹⁶O₂-saturated conditions. (d) Raman spectra of different systems. (e) Effect of process time on the Raman spectra. (f) MS₂ spectrum of intermediates from BA oxidation with ¹⁸O₂- and ¹⁶O₂-saturated conditions for BiN₃/MXene system.

Systematic isotope tracing experiments were also conducted to elucidate the origin of the generated HO[·] by employing benzoic acid (BA) as a chemical probe, which could selectively react with HO[·] to produce *p*-hydroxybenzoic acid (*p*-HBA). The observed peak at *m/z* = 140.12 in the MS₂ spectrum indicated the presence of *p*-HBA¹⁸OH, unequivocally revealing the generation of H¹⁸O[·] from the ¹⁸O₂-saturated solution (Fig. 5f). Correspondingly, the detection of *p*-HBA¹⁶OH at *m/z* = 138.13 signified the formation of H¹⁶O[·] under the ¹⁶O₂-saturated conditions. Comparative examinations demonstrated that BiN₃/MXene could enhance the generation of oxygenated intermediates, consequently facilitating the subsequent conversion to HO[·].

DFT calculations were further performed to determine the fundamental reaction mechanism that led to the increased activation of O₂. Analysis of charge density differences revealed that electrons accumulated at the Bi atoms, indicating that electrons transfer from the Ti to the Bi atoms (Fig. S16). Based on calculations of the partial density of states (PDOS), a Bi-6p and Ti-3d had a wide range for sharing electrons, from −5.5 to −2.0 eV, in the BiN₃/MXene sample, further indicating the robust electronic interactions between the Bi and Ti atoms (Fig. 6a). Additionally, the intensity of Ti-3d near *E_f* was slightly greater than that of pure MXene, thereby enhancing the conductivity and electron transfer within BiN₃/MXene system. Notably, the PDOS calculations confirmed that the anti-bonding orbitals (π^*) of O-2p split into discrete levels after O₂ adsorption on the Bi-N₃ sites (Fig. 6b). Simultaneously, the intensity of the localized Bi-6p states decreased significantly, suggesting that the O-2p orbital interacted with the Bi-6p orbital to generate hybrid states near *E_f*. This interaction facilitated electron transport from the Bi-N₃ sites to O₂ molecules, adding to the strength and activation of the O₂ bond [20]. Additionally, the crystal orbital Hamilton populations (COHP) of O₂ attached to Bi-N₃ and MXene were also calculated (Fig. 6c). The integral COHP (ICOHP) analysis (Fig. 6d) showed that the

strength of the O–O bond of O₂ on the Bi-N₃ sites (-ICOHP = 0.19/0.21) was weaker than that on the MXene matrix (-ICOHP = 1.80/1.82), indicating O–O bond on Bi-N₃ sites was more susceptible to breaking and participating in ensuing reactions, explaining the easier O₂ activation and the lower activity barrier.

As shown in Fig. 6e, the free energy of the 3e[−] ORR pathway in BiN₃/MXene system is exothermic and spontaneous [46]. O₂ was firstly adsorbed on the surface active sites (*) of BiN₃/MXene, then *O₂ was reduced and protonated to *OOH, and H₂O₂ can be subsequently generated and chemically bound with * to form *H₂O₂. Calculations of free energy (ΔG) between the different electronic reaction steps revealed that the *H₂O₂ → *OH exhibited the greatest ΔG , suggesting that the rate-determine step (RDS) was the *OH desorption from active sites. Notably, the ΔG values of the *O₂ formation on Bi-N₃ sites and O vacancy were −0.04 and −2.75 eV, respectively, implying the generation of the adsorbed *O₂ was the initial RDS on pristine MXene. Moreover, ΔG in the final electronic step for the Bi-N₃ sites (-4.79 eV) was lower than that of O vacancy (-6.61 eV), indicating that the removal of *OH from the Bi-N₃ sites was more facile. The decreasing ΔG of the RDS proved that the desorption of *OH was very robust, and consequently enhanced the subsequent reactions and promoted the activity and kinetics of the 3e[−] ORR. To elucidate the redistribution of electrons in the system, differences in charge density were analyzed (Fig. 6f). After O₂ adsorption, the electron density primarily localized at the Bi-N₃ sites, while *O₂ exhibited the opposite behavior. Therefore, the O₂ activation originated from the hybridization of the Bi-6p and O-2p orbitals, facilitating electron transfer from the Bi site to generate HO[·]. The results of the DFT calculations were consistent with the spontaneous and abundant release of HO[·] from the active sites of the surfaces in the BiN₃/MXene system.

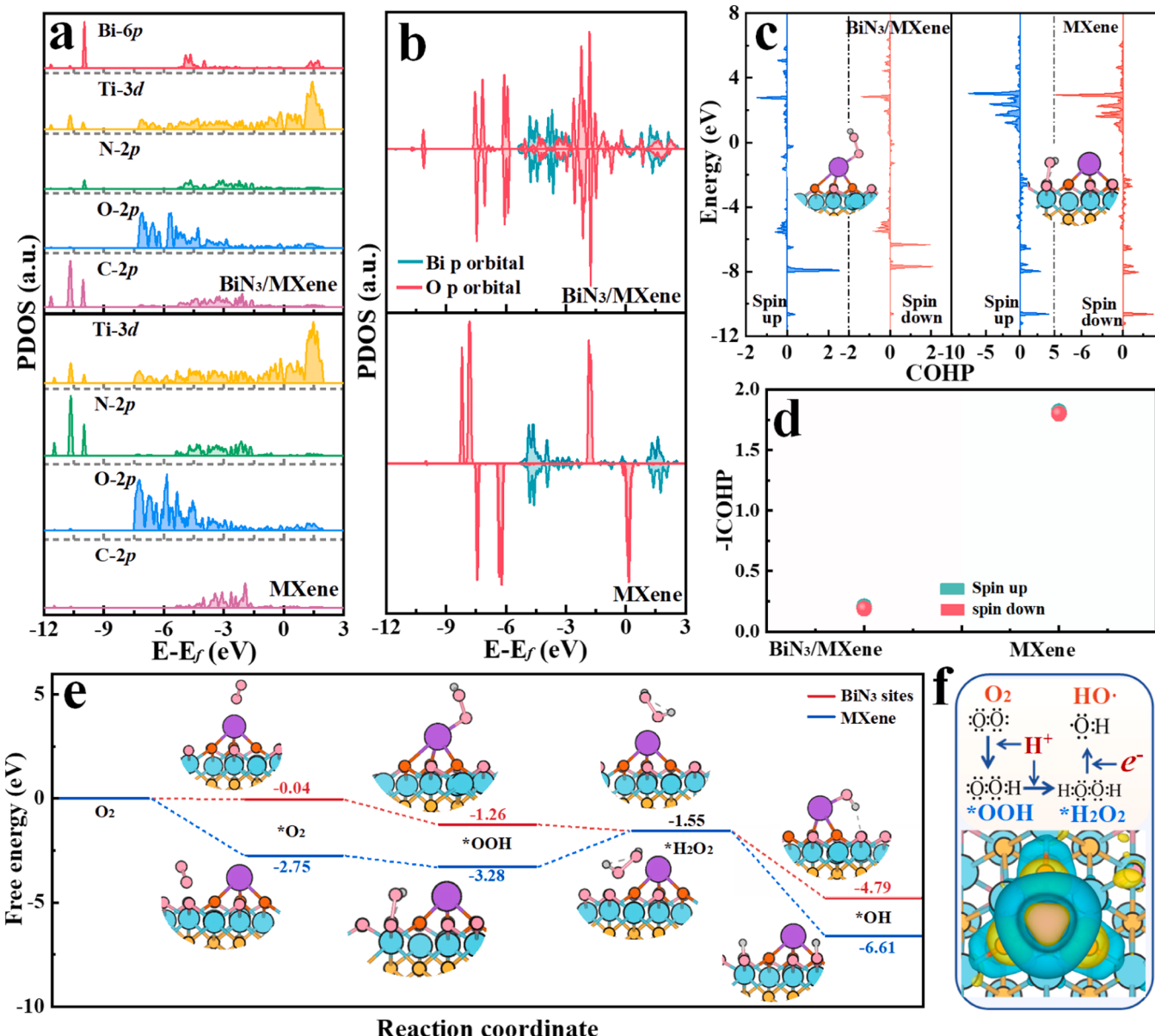


Fig. 6. Density-functional theory (DFT) calculations. (a) The PDOS of central atoms in BiN₃/MXene and MXene. (b) The PDOS of *O₂ adsorbed on BiN₃ and an O vacancy. (c) COHP of Ti–OOH and BiN₃–OOH. (d) The corresponding ICOHP values in (c). (e) Electron transfer system for the generation of *OH by O₂ activation. (f) Free energy diagram of the 3e⁻ ORR on BiN₃/MXene.

4. Conclusion

In summary, we developed a new approach that involves the selective electrochemical reduction of O₂ to HO[•] through a 3e⁻ ORR pathway, utilizing p-block Bi-SACs anchored on an N-doped MXene membrane. The experimental results and theoretical calculations indicated that the atomically dispersed Bi-N₃ sites with reactive p electrons that could facilitate the charge transfer and hybridize with the O-p orbitals. The robust electron interconnection markedly promoted the generation of *H₂O₂ intermediates through a 2e⁻ ORR pathway, thereby facilitating the selective and effective reduction to HO[•] via a 1e⁻ ORR pathway in the BiN₃/MXene electrocatalytic system. The cumulative HO[•] concentration under optimal conditions was as large as 26.7 μmol/(L·h·cm²) without requiring any additional chemical reagents. Importantly, the efficient generation of HO[•] was employed to preferentially degrade SMX with a kinetic constant ($k_{obs} = 1.027 \text{ min}^{-1}$) that was 5 ~ 40 × greater than that achieved with H₂O₂ activation, PMS activation, and traditional O₂ activation processes. This work offers valuable understanding into the

atomic-level creation of p-block SACs embedded in an electrocatalytic membrane to enhance the efficient generation and utilization of HO[•] for micropollutants degradation in wastewater.

CRediT authorship contribution statement

Limin Jin: Data curation, Investigation, Methodology, Writing – original draft. **Meng Liu:** Discussion, Supervision. **Shijie You:** Resources, Discussion. **Hongying Zhao:** Formal analysis. **Yanbiao Liu:** Investigation, Writing – review & editing, Funding acquisition.

Declaration of Competing Interest

The authors declare that they have no known competing financial interests or personal relationships that could have appeared to influence the work reported in this paper.

Data availability

Data will be made available on request.

Acknowledgements

Project supported by the Natural Science Foundation of Shanghai (no. 23ZR1401300) and the National Natural Science Foundation of China (no. 52170068 and 52325003).

Appendix A. Supporting information

Supplementary data associated with this article can be found in the online version at doi:10.1016/j.apcatb.2024.124044.

References

- [1] M. Bilal, S. Mehmood, T. Rasheed, H.M.N. Iqbal, Antibiotics traces in the aquatic environment: persistence and adverse environmental impact, *Curr. Opin. Environ. Sci. Health* 13 (2020) 68–74.
- [2] I.M. Dias, L.C. Mourão, L.A. Andrade, G.B.M. Souza, J.C.V. Viana, S.B. Oliveira, C. G. Alonso, Degradation of antibiotic amoxicillin from pharmaceutical industry wastewater into a continuous flow reactor using supercritical water gasification, *Water Res* 234 (2023) 119826.
- [3] L.M. Jin, M. Sun, J.P. Yang, Y.P. Huang, Y.B. Liu, Janus photoelectrocatalytic filter for sustainable water decontamination, *Appl. Catal. B Environ.* 339 (2023) 123150.
- [4] H. Sheng, A.N. Janes, R.D. Ross, H. Hofstetter, K. Lee, J.R. Schmidt, S. Jin, Linear paired electrochemical valorization of glycerol enabled by the electro-Fenton process using a stable NiSe₂ cathode, *Nat. Catal.* 5 (2022) 716–725.
- [5] S. Cheng, H. Zheng, C. Shen, B. Jiang, F.Q. Liu, A.M. Li, Hierarchical iron phosphides composite confined in ultrathin carbon layer as effective heterogeneous electro-Fenton catalyst with prominent stability and catalytic activity, *Adv. Funct. Mater.* 31 (2021) 2106311.
- [6] L.B. Xie, P.F. Wang, W.W. Zheng, S.H. Zhan, Y.G. Xia, Y.P. Liu, W.J. Yang, Y. Li, The strong metal-support interactions induced electrocatalytic three-electron oxygen reduction to hydroxyl radicals for water treatment, *Proc. Natl. Acad. Sci. USA* 120 (2023) e2307989120.
- [7] H. Kim, J. Lim, S. Lee, H.H. Kim, C. Lee, J. Lee, W. Choi, Spontaneous generation of H₂O₂ and hydroxyl radical through O₂ reduction on copper phosphide under ambient aqueous condition, *Environ. Sci. Technol.* 53 (2019) 2918–2925.
- [8] Y. Xu, Z. Mao, R. Qu, J. Wang, J. Yu, X. Luo, M. Shi, X. Mao, J. Ding, B. Liu, Electrochemical hydrogenation of oxidized contaminants for water purification without supporting electrolyte, *Nat. Water* 1 (2023) 95–103.
- [9] Y.B. Liu, J.H. Li, B.X. Zhou, J. Bai, Q. Zheng, J.L. Zhang, W.M. Cai, Comparison of photoelectrochemical properties of TiO₂-nanotube-array photoanode prepared by anodization in different electrolyte, *Environ. Chem. Lett.* 7 (2009) 363–368.
- [10] C. Choi, X. Wang, S. Kwon, J.L. Hart, C.L. Rooney, N.J. Harmon, Q.P. Sam, J.J. Cha, W.A. Goddard, M. Elimelech, H. Wang, Efficient electrocatalytic valorization of chlorinated organic water pollutant to ethylene, *Nat. Nanotechnol.* 18 (2023) 160–167.
- [11] H.L. Liu, Y.C. Ding, H.F. Tang, Y. Du, D.Y. Zhang, Y.H. Tang, C.B. Liu, Electrocatalytic deep dehalogenation of florfenicol using Fe-doped CoP nanotubes array for blocking resistance gene expression and microbial inhibition during biochemical treatment, *Water Res* 201 (2021) 117361.
- [12] S.C. Perry, D. Pangotra, L. Vieira, L.I. Csepei, V. Sieber, L. Wang, C. Ponce de León, F.C. Walsh, Electrochemical synthesis of hydrogen peroxide from water and oxygen, *Nat. Rev. Chem.* 3 (2019) 442–458.
- [13] D.L. Guo, S.J. You, F. Li, Y.B. Liu, Engineering carbon nanocatalysts towards efficient degradation of emerging organic contaminants via persulfate activation: a review, *Chin. Chem. Lett.* 33 (2022) 1–10.
- [14] A. Mehmood, M. Gong, F. Jaouen, A. Roy, A. Zitolo, A. Khan, M.T. Sougrati, M. Prims, A.M. Bonastre, D. Fongalland, G. Draicic, P. Strasser, A. Kucernak, High loading of single atomic iron sites in Fe–NC oxygen reduction catalysts for proton exchange membrane fuel cells, *Nat. Catal.* 5 (2022) 311–323.
- [15] D.Y. Zhang, Y.H. Tang, H.L. Liu, Z.M. Wang, X.X. Liu, H.F. Tang, H. Zhang, D. Y. Wang, Y. Long, C.B. Liu, Electrocatalytic deep dehalogenation and mineralization of florfenicol: synergy of atomic hydrogen reduction and hydroxyl radical oxidation over bifunctional cathode catalyst, *Environ. Sci. Technol.* 57 (2023) 20315–20325.
- [16] X.Q. Shen, F. Xiao, H.Y. Zhao, Y. Chen, C. Fang, R. Xiao, W.H. Chu, G.H. Zhao, In situ-formed Pd/Fe nanoalloy and carbon defects in cathode for synergic reduction–oxidation of chlorinated pollutants in electro-Fenton process, *Environ. Sci. Technol.* 54 (2020) 4564–4572.
- [17] Z.Y. Feng, Q.L. Tian, Q.Q. Yang, Y.B. Zhou, H.Y. Zhao, G.H. Zhao, Selectively photoelectrocatalytic reduction of oxygen to hydroxyl radical and singlet oxygen: mechanism and validation in coal wastewater, *Appl. Catal. B-Environ.* 286 (2021) 119908.
- [18] V. Giulimondi, S. Mitchell, J. Pérez Ramírez, Challenges and opportunities in engineering the electronic structure of single-atom catalysts, *ACS Catal.* 13 (2023) 2981–2997.
- [19] Y.N. Shang, X. Xu, B.Y. Gao, S.B. Wang, X.G. Duan, Single-atom catalysis in advanced oxidation processes for environmental remediation, *Chem. Soc. Rev.* 50 (2021) 5281–5322.
- [20] T.Z. Wang, X.J. Cao, H.Y. Qin, L. Shang, S.Y. Zheng, F. Fang, L.F. Jiao, P-block atomically dispersed antimony catalyst for highly efficient oxygen reduction reaction, *Angew. Chem. Int. Ed.* 60 (2021) 21237–21241.
- [21] A.E. Thorarinsdottir, C. Costentin, S.S. Veroneau, D.G. Nocera, P-block metal oxide noninnocence in the oxygen evolution reaction in acid: the case of bismuth oxide, *Chem. Mater.* 34 (2022) 826–835.
- [22] Z.Y. Teng, Q.T. Zhang, H.B. Yang, K. Kato, W.J. Yang, Y.R. Lu, S.X. Liu, C.Y. Wang, A. Yamakata, C.L. Su, B. Liu, T. Ohno, Atomically dispersed antimony on carbon nitride for the artificial photosynthesis of hydrogen peroxide, *Nat. Catal.* 4 (2021) 374–384.
- [23] Z.L. Jiang, T. Wang, J.J. Pei, H.S. Shang, D.N. Zhou, H.J. Li, J.C. Dong, Y. Wang, R. Cao, Z.B. Zhuang, W.X. Chen, D.S. Wang, J.T. Zhang, Y.D. Li, Discovery of main group single Sb–N₄ active sites for CO₂ electroreduction to formate with high efficiency, *Energy Environ. Sci.* 13 (2020) 2856–2863.
- [24] S. Liu, Z. Li, C. Wang, W. Tao, M. Huang, M. Zuo, Y. Yang, K. Yang, L. Zhang, S. Chen, P. Xu, Q. Chen, Turning main-group element magnesium into a highly active electrocatalyst for oxygen reduction reaction, *Nat. Commun.* 11 (2020) 938.
- [25] P.F. Li, F.Q. Yang, J. Li, Q. Zhu, J.W. Xu, X.J. Loh, K.W. Huang, W.P. Hu, J. Lu, Nanoscale engineering of p-block metal-based catalysts toward industrial-scale electrochemical reduction of CO₂, *Adv. Energy Mater.* 13 (2023) 2301597.
- [26] M. Alhabeb, K. Maleski, B. Anasori, P. Lelyukh, L. Clark, S. Sin, Y. Gogotsi, Guidelines for synthesis and processing of two-dimensional titanium carbide (Ti₃C₂T_x MXene), *Chem. Mater.* 29 (2017) 7633–7644.
- [27] L.M. Jin, X.G. Duan, M. Sun, C.D. Vecitis, H.Q. Yu, Y.B. Liu, A general strategy to synthesize fluidic single atom electrodes for selective reactive oxygen species production, *ACS Nano* 17 (2023) 12875–12883.
- [28] Y.F. Ren, Y.B. Liu, F.Q. Liu, F. Li, C.S. Shen, Z.C. Wu, Extremely efficient electro-Fenton-like Sb(III) detoxification using nanoscale Ti-Ce binary oxide: an effective design to boost catalytic activity via non-radical pathway, *Chin. Chem. Lett.* 32 (2021) 2519–2523.
- [29] C. Ma, S. Feng, J.M. Zhou, R.F. Chen, Y. Wei, H. Liu, S. Wang, Enhancement of H₂O₂ decomposition efficiency by the co-catalytic effect of iron phosphide on the Fenton reaction for the degradation of methylene blue, *Appl. Catal. B-Environ.* 259 (2019) 118015.
- [30] C.C. Dong, Z.Q. Wang, C. Yang, X.M. Hu, P. Wang, X.Q. Gong, L. Lin, X.Y. Li, Dual-functional single-atomic Mo/Fe clusters-decorated C₃N₅ via three electron-pathway in oxygen reduction reaction for tandemly removing contaminants from water, *Proc. Natl. Acad. Sci. USA* 120 (2023) e2305883120.
- [31] F. Li, P.F. Wang, T. Zhang, M.M. Li, S. Yue, S.H. Zhan, Y. Li, Efficient removal of antibiotic resistance genes through 4f-2p-3d gradient orbital coupling mediated Fenton-like redox processes, *Angew. Chem. Int. Ed.* 62 (2023) e202313298.
- [32] B. Ahmed, D.H. Anjum, Y. Gogotsi, H.N. Alshareef, Atomic layer deposition of SnO₂ on MXene for Li-ion battery anodes, *Nano Energy* 34 (2017) 249–256.
- [33] C.H. Jiang, Y.F. Fei, W.W. Xu, Z.K. Bao, Y.Z. Shao, S.J. Zhang, Z.T. Hu, J.G. Wang, Synergistic effects of Bi₂O₃ and Ta₂O₅ for efficient electrochemical production of H₂O₂, *Appl. Catal. B-Environ.* 334 (2023) 122867.
- [34] J. Wan, W. Chen, C. Jia, L. Zheng, X. Zheng, Y. Wang, W. Yan, C. Chen, Q. Peng, D. Wang, Y. Li, Defect effects on TiO₂ nanosheets: stabilizing single atomic site Au and promoting catalytic properties, *Adv. Mater.* 30 (2018) 1705369.
- [35] Y. Sun, D. Lu, H. Zhang, G. Liu, Y. Hu, H. Xie, J. Ma, Titanium oxide electrocatalytic membrane filtration: “Two faces” of oxygen vacancies in generation and transformation of reactive oxygen species, *Environ. Sci. Technol.* 57 (2023) 13226–13235.
- [36] V.K. Sharma, X. Ma, R. Zboril, Single atom catalyst-mediated generation of reactive species in water treatment, *Chem. Soc. Rev.* 52 (2023) 7673–7686.
- [37] D. Chodvadiya, P.K. Jha, B. Chakraborty, Theoretical inspection of Ni/α-six (X=N, P, As, Sb, Bi) single-atom catalyst: ultra-high performance for hydrogen evolution reaction, *Int. J. Hydrog. Energy* 47 (2022) 41733–41747.
- [38] Q. Chen, Y. Liu, Y. Lu, Y. Hou, X. Zhang, W. Shi, Y. Huang, Atomically dispersed Fe/Bi dual active sites single-atom nanozymes for cascade catalysis and peroxymonosulfate activation to degrade dyes, *J. Hazard. Mater.* 422 (2022) 126929.
- [39] E. Zhang, T. Wang, K. Yu, J. Liu, W. Chen, A. Li, H. Rong, R. Lin, S. Ji, X. Zheng, Y. Wang, L. Zheng, C. Chen, D. Wang, J. Zhang, Y. Li, Bismuth single atoms resulting from transformation of metal-organic frameworks and their use as electrocatalysts for CO₂ Reduction, *J. Am. Chem. Soc.* 141 (2019) 16569–16573.
- [40] H. Zhao, Y. Chen, Q. Peng, Q. Wang, G. Zhao, Catalytic activity of MOF(2Fe/Co)/carbon aerogel for improving H₂O₂ and •OH generation in solar photo-electro-Fenton process, *Appl. Catal. B-Environ.* 203 (2017) 127–137.
- [41] Y. Jiang, D. Baimanov, S. Jin, J. Cheuk Fung Law, P.C. Zhao, J.J. Tang, J. Peng, L. M. Wang, K.S.Y. Leung, W.C. Sheng, S.J. Lin, In situ turning defects of exfoliated Ti₃C₂ MXene into Fenton-like catalytic active sites, *Proc. Natl. Acad. Sci. USA* 120 (2023) e2210211120.
- [42] M. Bojtár, A. Kormos, K. Kis Petik, M. Kellermayer, P. Kele, Green-light activatable, water-soluble red-shifted coumarin photocages, *Org. Lett.* 21 (2019) 9410–9414.
- [43] M.M. Montemore, M.A. van Spronsen, R.J. Madix, C.M. Friend, O₂ activation by metal surfaces: implications for bonding and reactivity on heterogeneous catalysts, *Chem. Rev.* 118 (2018) 2816–2862.
- [44] F. Xiao, Z.N. Wang, J.Q. Fan, T. Majima, H.Y. Zhao, G.H. Zhao, Selective electrocatalytic reduction of oxygen to hydroxyl radicals via 3-electron pathway

with FeCo alloy encapsulated carbon aerogel for fast and complete removing pollutants, *Angew. Chem. Int. Ed.* 60 (2021) 10375–10383.

[45] X.M. Xu, Y.M. Zhang, Y. Chen, C.H. Liu, W.J. Wang, H.T. Huang, J. Y. Feng, Z.S. Li, Z.G. Zou, Revealing *OOH key intermediates and regulating H₂O₂ photoactivation by surface relaxation of Fenton-like catalysts, *Proc. Natl. Acad. Sci. USA* 119 (2022) e2205562119.

[46] H.J. Huang, D.S. Yu, F. Hu, S.C. Huang, J.N. Song, H.Y. Chen, L.L. Li, S.J. Peng, Clusters induced electron redistribution to tune oxygen reduction activity of transition metal single-atom for metal-air batteries, *Angew. Chem. Int. Ed.* 61 (2022) e202116068.